RSC Advances

PAPER

View Article Online
View Journal | View Issue

Cite this: RSC Adv., 2019, 9, 23334

$TiO_2@Sn_3O_4$ nanorods vertically aligned on carbon fiber papers for enhanced photoelectrochemical performance

Weiwei Xia,†[a] Haoyu Qian,†[a] Xianghua Zeng, *[ab] Jiawei Sun,[a] Pengdi Wang,[a] Min Luo[a] and Jing Dong[a]

Semiconductor heterostructures are regarded as an efficient way to improve the photocurrent in photoelectrochemical cell-type (PEC) photodetectors. To better utilize solar energy, $TiO_2@Sn_3O_4$ arrays vertically aligned on carbon fiber papers were synthesized *via* a hydrothermal route with a two-step method and used as photoanodes in a self-powered photoelectrochemical cell-type (PEC) photodetector under visible light. $TiO_2@Sn_3O_4$ heterostructures exhibit a stable photocurrent of 180 μA, which is a 4-fold increase with respect to that of the Sn_3O_4 nanoflakes on carbon paper, and a two-order increase with respect to that of the TiO_2 NRs arrays. The evolution of hydrogen according to the photo-catalytic water-splitting process showed that Sn_3O_4/TiO_2 heterostructures have a good photocatalytic hydrogen evolution activity with the rate of 5.23 μmol h^{-1}, which is significantly larger than that of Sn_3O_4 nanoflakes (0.40 μmol h^{-1}) and TiO_2 nanorods (1.13 μmol h^{-1}). Furthermore, the mechanism behind this was discussed. The detector has reproducible and flexible properties, as well as an enhanced photosensitive performance.

Received 23rd May 2019
Accepted 19th July 2019

DOI: 10.1039/c9ra03885j

rsc.li/rsc-advances

Introduction

TiO_2, as one of the widest band gap semiconductors (~3.0 eV), is widely used in photocatalysts and photoelectrodes due to its strong optical absorption, favorable band edge positions, and abundant availability.[1] For example, oriented, single-crystalline rutile TiO_2 nanorod films on transparent conductive fluorine-doped tin oxide (FTO) substrates or carbon fiber were used as dye-sensitized solar cells (DSSCs) and exhibited an improved cell performance due to a direct connection of the point of photogeneration with the collection electrode.[2,3] However, the energy unitization efficiency of TiO_2 is limited because of its wide band gap and the rapid recombination of photogenerated electron–hole pairs. Metal/nonmetal element doping or decoration was developed to increase its photoactivity, for example, TiO_2 modification with carbon nanolayers used as a photocatalyst led to an enhanced efficiency due to the increased substrate adsorption in the vicinity of the photocatalytic sites and high migration efficiency of photoinduced electrons at the carbon/TiO_2 interface.[4,5] And metal modification of TiO_2 to increase photocatalytic properties of nanoparticles were reported also.[6,7]

Among their methods, heterogeneous photocatalysts were regarded as an effective way to improve photocatalytic activity, since heterojunctions can promote charge migration across both the semiconductor/electrolyte and the semiconductor/photoelectrode interface effectively separating photogenerated electrons and holes.[8–10] P-SnO/*n*-TiO_2 composite electrodes revealed a better PEC performance as reported by Naeem *et al.*[11] And tree-like TiO_2 architectures assembled with CdS and reduced graphene oxide can improve photoelectrochemical performance as reported by Pathak *et al.*[12]

On the other hand, a mixed-valence tin oxide (Sn^{2+} and Sn^{4+}) has a strong resistance against acidic/alkaline solutions and exhibits a good photocatalytic activity without generating secondary pollutants under irradiation with visible light. It is a desirable material for PEC-type photodetectors and an efficient visible-light-driven photocatalyst.[13–16] To improve the photoelectric properties, Sn_3O_4 nanomaterials combined with others have been used as electrodes and photocatalysts. For example, integrated Sn_3O_4 nanosheets and rGO nanosheets as hybrid nanostructures were used as high-performance photocatalysts.[17] With the combination of visible light active Sn_3O_4 and ultraviolet (UV) light active TiO_2, this composite can be a broad spectrum photocatalytic material from the UV to visible region as well as having enhanced separation of photogenerated electrons and holes,[18] therefore people paid more attention to $TiO_2@Sn_3O_4$ nanostructures. For example, 3D lupinus-like $TiO_2@Sn_3O_4$ nanostructures on a transparent F-doped SnO_2 (FTO) glass substrate were prepared and used as photoanode for PEC water splitting as reported by Zhu *et al.*[19] $TiO_2@Sn_3O_4$ hybrid nanobelts exhibited markedly enhanced photoelectrochemical (PEC) response, which caused higher

---

[a] College of Physics Science and Technology, Institute of Optoelectronic Technology, Yangzhou University, Yangzhou 225002, P. R. China. E-mail: xhzeng@yzu.edu.cn; wwxia@yzu.edu.cn

[b] College of Electrical, Energy and Power Engineering, Yangzhou 225127, P. R. China

† W. X. and H. Q. contributed equally to this work.

photocatalytic hydrogen evolution even without the assistance of Pt as a co-catalyst, and enhanced the degradation ability of organic pollutants under both UV and visible light irradiation.[20]

Recently, self-powered photodetectors (SPPD) are becoming a promising candidate for application in high-sensitivity and high-speed SPPDs because they do not require batteries as an external power source.[21,22] For example, TiO_2 based self-powered photochemical UV detectors have been reported, but they are restricted to UV light.[23–25] To better use solar light for energy conversion, it is very important to extend the spectrum to the visible region. Although there are some discussions on the TiO_2@Sn_3O_4 electrodes, flexible SPPDs based on TiO_2@Sn_3O_4 haven't been reported yet.

Herein, TiO_2 nanorod arrays (NRs) vertically aligned on the carbon fiber papers were synthesized *via* a hydrothermal route, where TiO_2 nanorods have a diameter of about 500–1000 nm; then Sn_3O_4 nanoflakes (NFs) with a thickness of less than 100 nm and width of 100–300 nm were grown on the surface of TiO_2 nanorod. Furthermore, hybrid PEC-type photodetectors were designed using three prepared 3-D (three dimensional) hierarchical arrays, TiO_2, Sn_3O_4 and TiO_2@Sn_3O_4 as photoanodes, respectively. As a visible light SPPD device, TiO_2@Sn_3O_4 heterostructures exhibit a stable photocurrent of 180 μA, which is a 4-fold increase with respect to that of Sn_3O_4 NFs on carbon paper, and a two-order increase with respect to that of TiO_2 NRs on carbon paper. The detector exhibits reproducible and flexible properties, as well as an enhanced photosensitive performance. Finally, the photocatalytic properties of the pure Sn_3O_4, TiO_2 NRs and their combinations have been studied, where the evolution of hydrogen was measured according to the photocatalytic water-splitting process. The results show that Sn_3O_4/TiO_2 heterostructures have hydrogen evolution activity with the rate of 5.23 μmol h^{-1}, significantly larger than that of others. The mechanism behind has been discussed.

Experimental section

Materials

All chemicals were analytical-grade and used without further purification. Titanium butoxide ($Ti(OC_4H_9)_4$), tin dichloride dehydrate ($SnCl_2\cdot 2H_2O$), sodium citrate dihydrate ($Na_3C_6H_5O_7\cdot 2H_2O$, 99%), ethanol, and hydrochloric acid (HCl, 36.5–38% by weight) were purchased from Sinopharm Chemical Reagent Co., Ltd. Commercial carbon fiber papers were provided by FuelCellStore.

Synthesis of TiO_2 NRs

TiO_2 nanorod arrays (NRs) were prepared on the carbon fiber papers by the one-step hydrothermal method. Firstly, the commercial carbon fiber papers were cut into the desired sizes and ultrasonically washed using deionized water and ethanol. Then, 12 mL of deionized water was mixed with 12 mL of hydrogen chloride (36.5–38% by weight). The mixture was stirred for 5 min before the addition of 400 μL of titanium butoxide (97% Aldrich). After stirring for another 5 min, the mixture was transferred into a 50 mL Teflon-lined stainless steel autoclave with the treated carbon fiber paper vertically immersed in the reaction solution. The hydrothermal reaction was carried out at 180 °C for 18 h and cooled naturally to room temperature. Finally, the carbon fiber paper substrates covered by TiO_2 NRs were washed with deionized water.

Synthesis of Sn_3O_4 NFs

Sn_3O_4 nanoflakes (NFs) were prepared on the carbon fiber papers by a modified hydrothermal approach, which is similar to the reported in our previous study.[26] In detail, 1.073 g of $SnCl_2\cdot 2H_2O$ and 2.940 g $Na_3C_6H_5O_7\cdot 2H_2O$ were dissolved in the mixture of 20 mL de-ionized water and 20 mL alcohol under constant magnetic stirring for approximately 60 min. The obtained homogeneous solution was transferred into a Teflon liner of 50 mL capacity with the carbon fiber paper vertical immersed into the reaction solution and keeping sealed under 180 °C for 18 h. After the reaction, the carbon fiber paper coated with a brown product was further washed with deionized water and absolute ethanol for several times. The final sample dried in an oven before characterization.

Synthesis of TiO_2@Sn_3O_4 hierarchical heterostructured arrays

Details of growth process of the TiO_2@Sn_3O_4 hierarchical heterostructured arrays were described previously. 0.35 g of $SnCl_2\cdot 2H_2O$ and 1.14 g of $Na_3C_6H_5O_7\cdot 2H_2O$ were dissolved in a mixture of 25 mL of deionized water and 25 mL of alcohol under constant magnetic stirring for approximately 60 min. Then, the mixture was transferred to a Teflon-lined autoclave (50 mL). Subsequently, the carbon fiber paper covered by TiO_2 NRs was vertically immersed into the aforementioned mixture. The hydrothermal reaction was carried out at 180 °C for 18 h and cooled naturally to room temperature. Finally, the resulting carbon fiber papers with TiO_2@Sn_3O_4 hierarchical heterostructured arrays were rinsed with deionized water and dried at 60 °C in air.

Characterization

The morphology and microstructure of the TiO_2@Sn_3O_4 heterostructured nanowire arrays on carbon fiber papers were examined by a Hitachi S-4800 field emission scanning electron microscope (FESEM) and a Tecanai G2 F30 field emission transmission electron microscope (TEM) operated at an accelerating voltage of 300 kV. The phase and composition of samples were analyzed by powder X-ray diffraction (XRD, Bruker D8 advance) with Cu Kα ($\lambda = 1.5406$ Å). UV-visible absorption spectra (200–1200 nm) were measured using a Varian Cary 50 UV-visible spectrophotometer. X-ray photoelectron spectroscopy (XPS) was conducted on an ESCALAB-250Xi photoelectron spectroscope to obtain information on the valence state of the Ti and O ions.

PEC measurements

To perform the PEC tests, the Zanner CIMPS electrochemical workstation (Germany) was used to examine the photocurrent densities' curves and electrochemical impedance spectroscopy

(EIS) plots in a three-electrode mode. PEC measurements were performed in 0.1 M Na_2SO_4 using Pt wire as the counter electrode and Ag/AgCl in saturated KCl as a reference electrode. The carbon fiber papers with $TiO_2@Sn_3O_4$ hierarchical heterostructured arrays were acted as the working electrode and placed in the cell with an area of 1 × 1 cm^2 exposed to the electrolyte. A 500 W Xe lamp (CEL-HXF 300, Beijing Au-light, China) was employed as incident light source to study the PEC response of the samples. The H_2 evolution experiments were carried out in a gas-closed circulation system under a 300 W Xe lamp.

Results and discussion

Morphology and structure

The schematic diagram of the formation process of the $TiO_2@Sn_3O_4$ hierarchical heterostructured nanowire arrays on carbon fiber papers is shown in Fig. 1a, which involves two major steps. In the first step, large-scale well-aligned TiO_2 nanowires are grown on the carbon fiber papers by the one-step hydrothermal method. High-density TiO_2 NRs are grown uniformly on the carbon fiber papers, which also serve as stems to provide a platform for later Sn_3O_4 NFs growth. In the second step, the Sn_3O_4 NFs were conformably coated onto TiO_2 nanowire stems by a facile and effective hydrothermal method. Fig. 1b reveals the crystal structure of the as-synthesized TiO_2, Sn_3O_4 and $TiO_2@Sn_3O_4$ nanowires heterostructure arrays on carbon fiber papers. The diffraction peaks in each pattern at 26.22° and 54.72° are indexed to the carbon fiber paper substrate. For TiO_2 NRs on the carbon fiber paper substrate, the diffraction peaks at 2θ values of 27.45°, 36.08°, 41.22°, 44.05°, 56.64°, 62.74°, 64.04°, 69.01° and 69.79° can be well identified as (110), (101), (111), (210), (220), (002), (310), (301) and (112) planes of the tetragonal rutile TiO_2 phase (JCPDS 21-1276). Diffraction peaks at about 33.01°, 37.07° and 51.69° can be indexed to (210), (130) and $(\bar{1}\bar{3}2)$ phases of Sn_3O_4 (JCPDS 16-0737). Besides, the XRD pattern of as-synthesized $TiO_2@Sn_3O_4$ hierarchical nanowire arrays on carbon fiber papers is also shown in Fig. 1c. All the major diffraction peaks of TiO_2 and Sn_3O_4 can also be identified in the pattern of $TiO_2@Sn_3O_4$ hierarchical structure and no extra peak was detected.

To observe the morphology and microstructure of the samples, the FESEM images of TiO_2 NRs and $TiO_2@Sn_3O_4$ hierarchical structure are shown in Fig. 2. Fig. 2a–c show FESEM images of TiO_2 NRs on carbon fiber paper substrate with different magnifications. With the hydrothermal synthesis, TiO_2 NRs with a size of 500–1000 nm grow vertically along the surface of the carbon fiber paper substrate forming nanowire arrays with good uniformity, each TiO_2 NR has a square shape. After the growth of Sn_3O_4 nanoflake branches by the followed hydrothermal method, it can be obviously noted that high-density secondary Sn_3O_4 nanoflake branches are successfully grown on the surface of the TiO_2 nanowires with good uniformity, which lead to a thicker and rougher surface of TiO_2 nanowires. The magnified image (Fig. 2f) reveals that Sn_3O_4 NFs have a thickness of less than 100 nm and width of 100–300 nm. Because of the existence of convenient diffusion pathways, these $TiO_2@Sn_3O_4$ nanowire array hierarchical structures are extraordinarily accessible to electrolytes during the electrochemical measurement process. In addition, the compact nanoflakes interlaced with each other can also greatly increase the capture of light. Further morphological and structural characterizations of the $TiO_2@Sn_3O_4$ hierarchical structure are performed using HRTEM. The low-magnification TEM image (Fig. 3a) reveals the typical heterostructured nanowire taken from hierarchical $TiO_2@Sn_3O_4$ nanowire arrays, which can be evidently observed that the individual TiO_2 nanowire with a length of several micrometers is covered by compact Sn_3O_4 nanoflake branches. A close examination of the exposed profile (inset of Fig. 3a) reveals that thickness of the outer Sn_3O_4 NFs is around several tens nm. The high resolution TEM examination shown in Fig. 3b reveals a distinct set of visible lattice fringes of 0.33 nm, corresponding to the (111) plane of triclinic Sn_3O_4 (JCPDS 16-0737). To determine the atomic distribution in $TiO_2@Sn_3O_4$ hierarchical structure, EDS element mapping analysis of the individual hybrid nanowire was performed (Fig. 3c–f), Ti, Sn and O elements are found clearly in the hierarchical heterostructure of $TiO_2@Sn_3O_4$ nanowire.

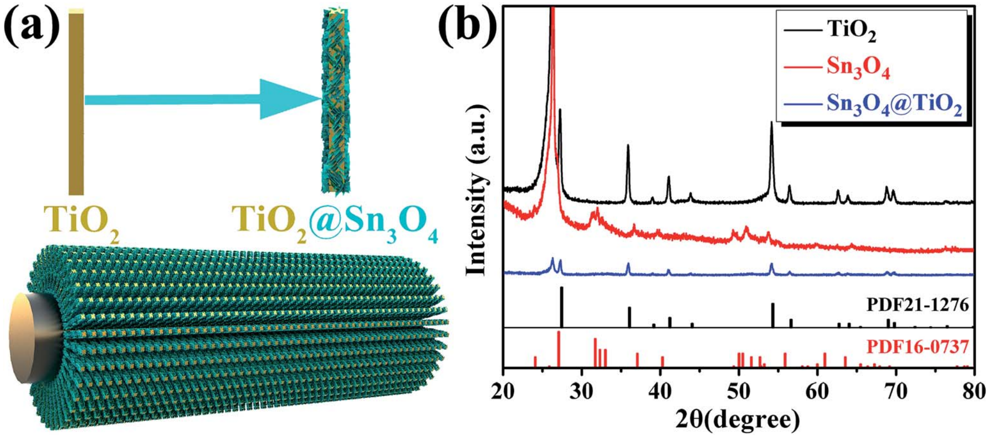

Fig. 1 (a) Schematic of fabrication process and (b) XRD patterns of TiO_2 NRs, Sn_3O_4 NFs and $TiO_2@Sn_3O_4$ heterostructure arrays grown on carbon fiber papers.

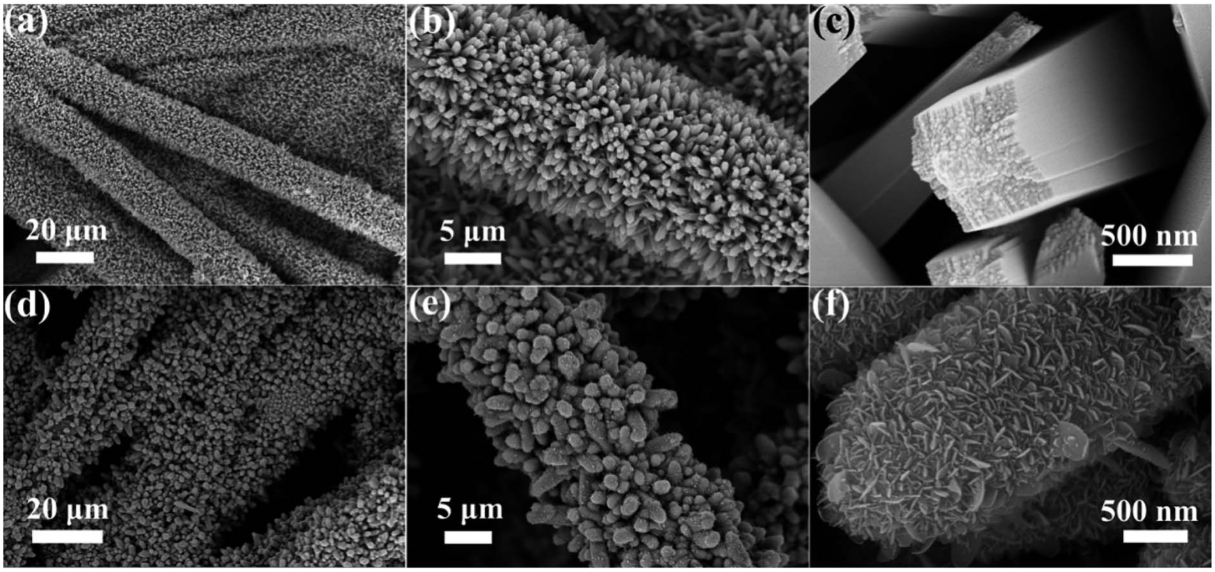

Fig. 2 FESEM images of (a–c) TiO_2 NRs and (d–f) TiO_2@Sn_3O_4 hierarchical structure grown on carbon fiber paper.

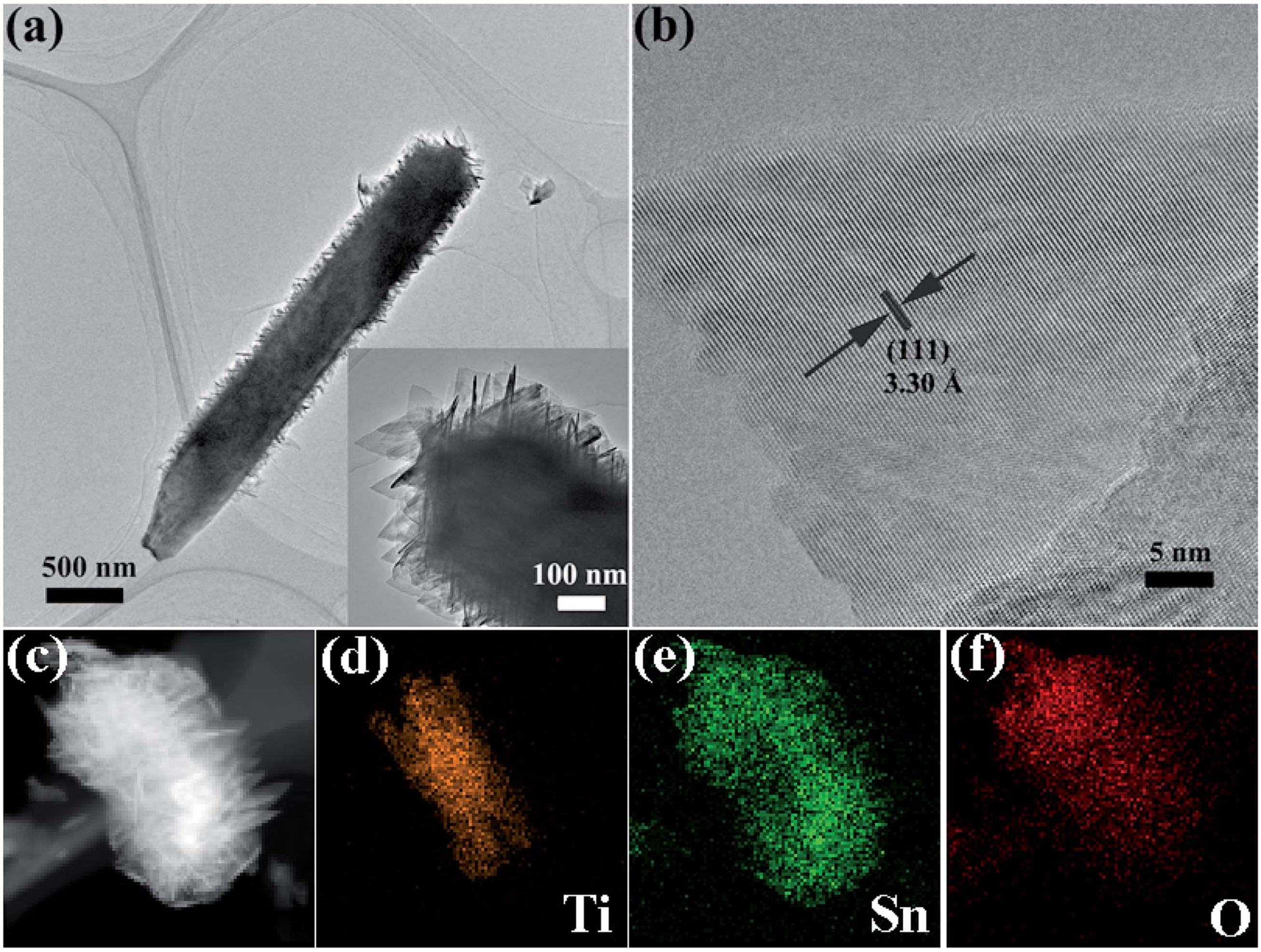

Fig. 3 TEM image (a) and HRTEM image (b) of a representative TiO_2@Sn_3O_4 heterostructured nanowire. (c–f) Elemental mapping images of an individual hybrid nanowire.

Optical properties of the as-prepared TiO_2 NRs, Sn_3O_4 NFs and $TiO_2@Sn_3O_4$ hierarchical structure grown on carbon fiber paper were investigated by diffuse reflectance UV-vis spectra (ultraviolet-visible spectroscopy) (Fig. 4a). Compared with bare TiO_2 NRs, $TiO_2@Sn_3O_4$ hierarchical structure shows significantly increased light absorption in the visible-light region. The absorption edge of the TiO_2 NRs (black line) is located at 408 nm, which indicates the energy gap is 3.04 eV. The absorption band edge of the Sn_3O_4 NFs (red) is closed to 435 nm (with the energy gap of 2.85 eV), which can absorb the visible light. For the 3D $TiO_2@Sn_3O_4$ hierarchical structure (blue line), its absorption band edge is at ~558 nm, showing a significant redshift compared with the bare TiO_2 NRs. Therefore, coupling TiO_2 NRs with Sn_3O_4NFs can significantly broaden the range of photo-response, which can result in an enhancement of utilization of solar light and improved PEC performance. XPS measurements were used to investigate the surface composition of the as-synthesized products. Fig. 4b shows the XPS survey spectra of Sn_3O_4 NFs and $TiO_2@Sn_3O_4$ hierarchical structure. Chemical state binding energy of Sn 3d in the Sn_3O_4 NFs and $TiO_2@Sn_3O_4$ hierarchical structure was carried by XPS measurements as shown in Fig. 4c. Consistent with our previous study, the binding energies of Sn $3d_{3/2}$ and Sn $3d_{5/2}$ peaks in the pure Sn_3O_4 NFs locate at 494.64 eV and 486.15 eV, respectively. After growing onto the TiO_2 NRs, however, the Sn $3d_{3/2}$ and Sn $3d_{5/2}$ peaks of $TiO_2@Sn_3O_4$ hierarchical structure obviously shifted to higher binding energies by 0.46 and 0.47 eV, respectively. Therefore, the observed peak shift indicates that the electrons are injected from Sn_3O_4 NFs to the TiO_2 NRs in $TiO_2@Sn_3O_4$ hierarchical structure. This result can be further supported by the shift by 0.4 eV of the Ti $2p_{3/2}$ peak in Fig. 4d. The $TiO_2@Sn_3O_4$ hierarchical structure is possibly advantageous because of their electronic band structure.

Table 1 Energy level

Samples	E_g (eV)	E_C (eV *vs.* vacuum)	E_F (eV *vs.* vacuum)	E_v (eV *vs.* vacuum)
TiO_2	3.04	4.43	5.20	7.47
Sn_3O_4	2.85	3.7	3.9	6.55

UPS measurements were carried out to study the surface electron behavior of TiO_2 NRs, as shown in Fig. 4e and f. Fig. 4e is a view of the secondary electron edge (SEE) energy corresponding to the left spectra in UPS data. The work function (ϕ) can be by observing the low energy secondary electron cutoff, which is ~5.20 eV for TiO_2 NRs. Fig. 4f is a view of the valence band maximum (VBM) region corresponding to the right spectra in UPS data and the VBM can be extracted from the Fig. 4f, which is about 2.2 eV for TiO_2 NRs. The energy band of Sn_3O_4 NFs has been discussed previously.[22] Then, the conduction band and valence band (*vs.* vacuum) of TiO_2 NRs and Sn_3O_4 NF scan be obtained, as shown in Table 1.

The PEC measurements were carried out in a three-electrode configuration in 0.1 M Na_2SO_4 using Pt wire as a counter electrode, Ag/AgCl in saturated KCl as a reference electrode, and carbon-paper-supported Sn_3O_4 NFs, TiO_2 NRs and $TiO_2@Sn_3O_4$ hierarchical structures as active photoanodes, respectively, as shown in the Fig. 5a. The incident radiation is switched with an on/off interval of 20 s. Twenty repeated cycles are displayed in

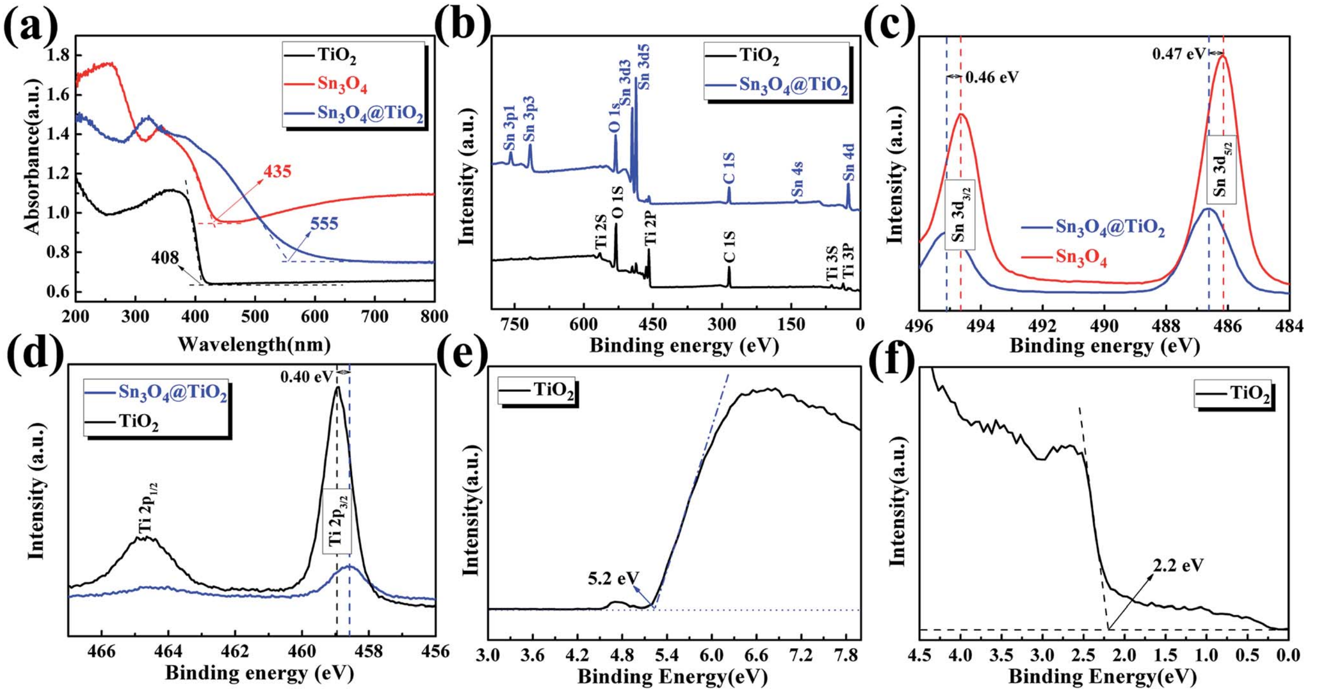

Fig. 4 (a) UV-vis spectra of the TiO_2 NRs and $TiO_2@Sn_3O_4$ hierarchical structure. (b) Survey XPS spectra of TiO_2 NRs and $TiO_2@Sn_3O_4$. (c) XPS spectra of Sn 3d for Sn_3O_4 NFs and $TiO_2@Sn_3O_4$. (d) XPS spectra of Ti 2p for Sn_3O_4 NFs and $TiO_2@Sn_3O_4$. (e) UPS secondary edge spectrum and (f) view of the valence band maximum (VBM) region.

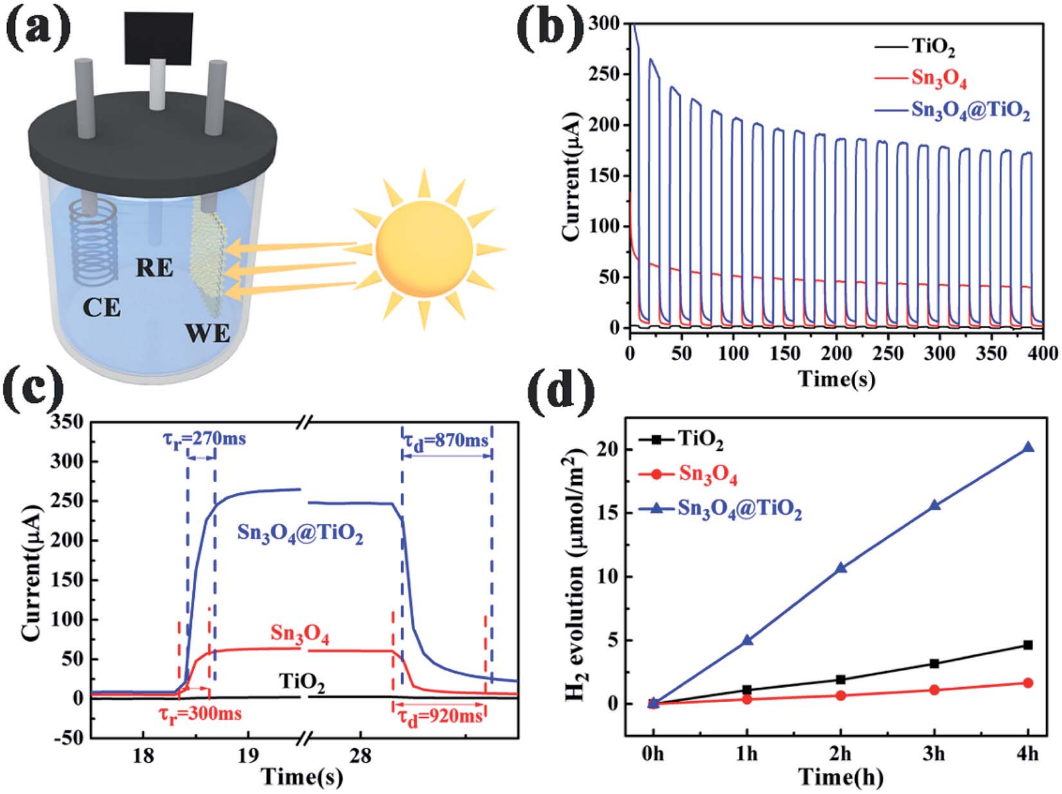

Fig. 5 (a) Schematic illustration of self-powered PEC type detector; (b) photocurrent responses under on/off of 20 s for 20 cycles at 0.0 V *versus* Ag/AgCl with illumination of 500 W Xe lamp; (c) enlarged rising and decaying edges of the photocurrent response; (d) H_2 evolutions as a function of time under irradiation of the 500 W Xe arc lamp.

Fig. 5b, in which TiO_2 NRs display a quite weak photocurrent under visible-light irradiation. The as-obtained Sn_3O_4 NFs exhibit a much enhanced photocurrent density of ~40 μA cm^{-2} in the visible-light spectral region. However, the photocurrent exhibited nearly 40% decrease after 20 cycles. The TiO_2@Sn_3O_4 hierarchical electrode shows the highest photocurrent and a decrease of 30% compared with the initial photocurrent. From the magnified rising and decaying edges of photocurrent shown in Fig. 5c, a fast photo-response can be seen clearly. The rising time (τ_r, defined as the time to increase from 10% to 90% of the maximum photocurrent) and the decaying time (τ_d, defined as the time to recover from 90% to 10% of the maximum photocurrent) of TiO_2@Sn_3O_4 hierarchical electrodes are about 0.27 s and 0.87 s, respectively, faster than 0.30 s and 0.92 s for Sn_3O_4 NFs. The mechanism of reason for enhanced PEC performance will be explained in detail later. PEC measurements that the 3D TiO_2@Sn_3O_4 photoelectrode exhibited a stable photocurrent of 180 μA, which is 4-fold increase with respect to that of Sn_3O_4 NFs, and two-order increase respect to that of TiO_2 NRs. In comparison to the report of ref. 19, the formation of the heterostructure on the photocurrent is much larger without external power source.

Furthermore, the photocatalytic property of the pure Sn_3O_4, TiO_2 NRs and their combinations have been studied under visible light, where the evolution of hydrogen was measured according to the photo-catalytic water-splitting process, as shown in Fig. 5d. The results show that Sn_3O_4 NFs show negligible photocatalytic hydrogen evolution activity with the rate of 0.40 μmol h^{-1} cm^{-2} and the rate of the TiO_2 NRs is 1.13 μmol h^{-1} TiO_2 NRs, which is much lower than that of Sn_3O_4/TiO_2 heterostructures of 5.23 μmol h^{-1}, this value is comparable with the results reported by Kodiyath *et al.*[27] Contrary to the photocurrents, the H_2 generation of Sn_3O_4 is less than that of TiO_2. Several aspects, such as the density of the photoanode catalysts, electron transportation and carrier's concentration *etc.*, will influence the H_2 generation. In the further work we will study them.

To further understand the reasons of the charge transfer process occurring at the interface of photoelectrode/electrolyte, electrochemical impedance spectroscopy (EIS)[28,29] was carried out and presented in Fig. 6a and b. The equivalent RC circuit was used to interpret the EIS results (see inset of Fig. 6b). As shown in Fig. 6a and b, each Nyquist plots are composed of one semicircle and a slope line. For deeper analysis, all Nyquist plots display a semicircle at high frequencies whose diameter represents the charge-transfer resistance (R_{ct}), which reflects the electron transfer kinetics of the redox probe at the interface. The slope line at low frequency is related to the diffusion process. The corresponding equivalent circuit is depicted in the inset of Fig. 6b, where R_s denotes the series resistance at the interface of the photoelectrode material and the carbon fiber paper substrate, C_{d1} reflects the constant phase element that models capacitance of the double layer, and Z_w stands for the Warburg impedance originated from the diffusion process at

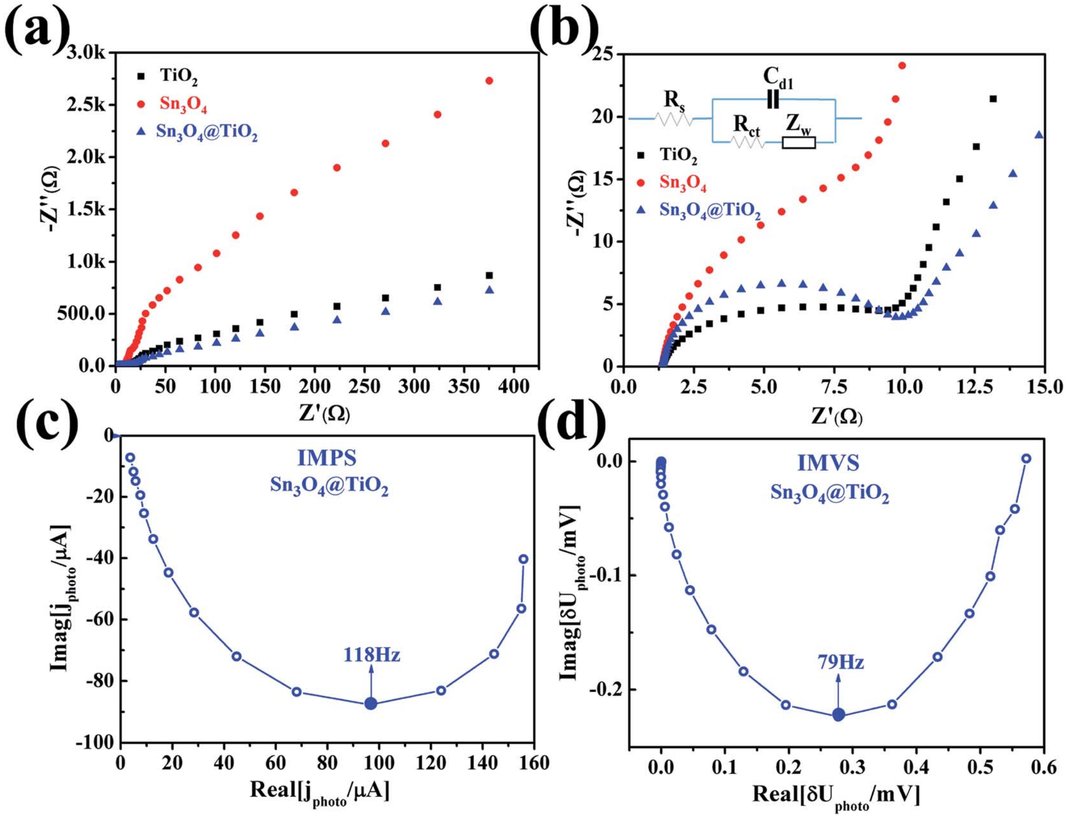

Fig. 6 (a) Nyquist plots of TiO_2 NRs, Sn_3O_4 NFs and TiO_2@Sn_3O_4 heterostructure arrays grown on carbon fiber papers; (b) plots in the expanded high-frequency region and the inset represents the equivalent circuit applied to fit the impedance data; (c) typical IMPS and (d) IMVS plot of TiO_2@Sn_3O_4 heterostructure arrays.

the electrode surface. After being decorated with Sn_3O_4 NFs, the value R_{ct} of TiO_2@Sn_3O_4 hierarchical photoelectrode is almost the same, which is smaller than the corresponding value of Sn_3O_4 NFs. The above result demonstrates that TiO_2 NRs provide a conduction path and rapidly transfer the photoelectrons coming from Sn_3O_4 NFs to the carbon fiber paper substrate along the vertically oriented TiO_2 NRs, which is also correlated to the enhanced PEC performance. To obtain deep insights into the enhanced PEC properties of the TiO_2@Sn_3O_4 hierarchical electrodes, intensity modulated photocurrent spectroscopy (IMPS) and intensity modulated photovoltage spectroscopy (IMVS) have been employed to investigate further the electron transport and recombination process, as shown in Fig. 6c and d. The IMPS and IMVS plots display a semicircle in the complex plane under the incident light source was an LED with a wavelength of 564 ± 60 nm. From the IMPS measurement (Fig. 6c), the transport time (τ_d) of injected electrons from Sn_3O_4 NFs to TiO_2 NRs can be calculated from the following equation:

$$\tau_d = 1/(2\pi f_{d,min}),$$

where $f_{d,min}$ is characteristic frequency at the minimum of the IMPS imaginary component. Thus, τ_d value is estimated to be 1.35 ms. In addition, from the IMVS measurement (Fig. 6d), the recombination lifetime (τ_n) was determined using the following equation:

$$\tau_n = 1/(2\pi f_{n,min}),$$

where $f_{n,min}$ is the characteristic frequency at the minimum of IMVS imaginary component. The τ_n can be calculated to be 2.0 ms for TiO_2@Sn_3O_4 hierarchical photoelectrode. All the above results indicate that vertically oriented TiO_2 NRs can serve as fast electron transport and TiO_2@Sn_3O_4 heterostructure can increase electron lifetime and result in the enhanced PEC performance.

Based on the above measurements and analyses, by combining both the band gap estimated from optical absorption and the conduction band and valence band (*vs.* vacuum) obtained by UPS, the energy band alignment of TiO_2 NRs and Sn_3O_4 NFs is displayed in Fig. 7a. When Sn_3O_4 NFs contact with TiO_2 NRs to form a heterojunction, the band structure of TiO_2@Sn_3O_4 is reconfigured. The bandgap energy of Sn_3O_4 (2.85 eV) is smaller than TiO_2 (3.04 eV) and both the potentials of VB and CB of Sn_3O_4 are higher than those of TiO_2, so TiO_2@Sn_3O_4 heterostructure belongs to a typical type-II heterojunction. Under visible-light irradiation, photogenerated holes and electrons appear in the VB and CB of Sn_3O_4 NFs. Due to type-II heterostructure, the photogenerated electrons in Sn_3O_4 CB were easily injected into the TiO_2 CB. Effective separation of photoexcited electron–hole pairs could be accomplished by a longer electron lifetime. To explain the enhanced PEC performance of TiO_2@Sn_3O_4 photoelectrode in the visible-light

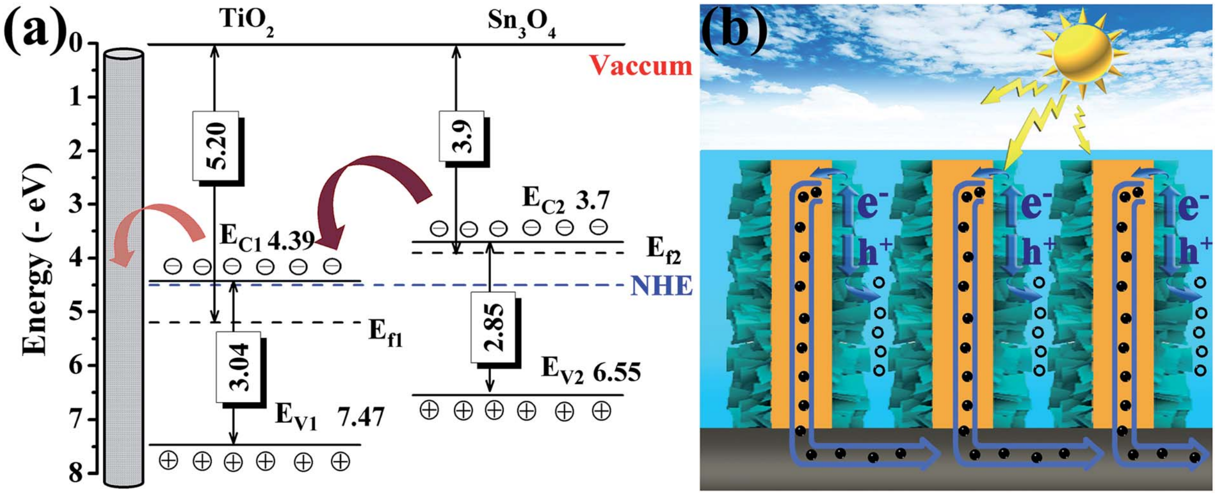

Fig. 7 (a) Proposed energy band alignment and (b) scheme of the electron–hole pair separation and the transfer process in TiO_2@Sn_3O_4 photoelectrode.

spectral region, we present the scheme of the electron–hole pair separation and the transfer process in TiO_2@Sn_3O_4 hierarchical photoelectrode (Fig. 7b). Generally, enhanced PEC performance of TiO_2@Sn_3O_4 photoelectrode may be attributed to the reasonable design of TiO_2NRs @Sn_3O_4NFs heterostructure. On one hand, the aligned TiO_2 NRs can provide a conduction path and rapidly transfer electrons to carbon fiber paper substrate along the vertically oriented TiO_2 NRs. On the other hand, the type-II heterojunction of TiO_2@Sn_3O_4 heterostructure can drive photoexcited electron transfer from Sn_3O_4 NFs to TiO_2 NRs. In one word, for our TiO_2@Sn_3O_4 photoelectrode under the synergistic effects between unique band structures and morphology, which is crucial for the enhancement of PEC performance.

Conclusion

In this paper, TiO_2@Sn_3O_4 arrays vertically aligned on the carbon fiber papers were synthesized and used as photoanodes to improve the photocurrent performance under visible light. Because of the 3-D structure, the TiO_2@Sn_3O_4 arrays can absorb more incident lights which have been reflected among Sn_3O_4 NFs, at same time there are more interfacial states to adsorb electrolyte molecules. The TiO_2@Sn_3O_4 arrays not only extend the spectra from UV to visible region with respect to TiO_2, but also increase the separation of photogenerated electrons and hole due to the good band alignment of type-II heterostructure for TiO_2@Sn_3O_4. Therefore, as photoanodes in self-powered photoelectrochemical cell-type (PEC) photodetector under visible light, TiO_2@Sn_3O_4 heterostructures exhibit a stable photocurrent of 180 μA, which is 4-fold increase with respect to that of Sn_3O_4 NFs, and two-order increase respect to that of TiO_2 NRs arrays. Sn_3O_4/TiO_2 heterostructures also have a good photocatalytic hydrogen evolution activity with the rate of 5.23 μmol h^{-1}, which is quite larger than that of Sn_3O_4 nanoflakes (0.40 μmol h^{-1}) and TiO_2 NRs (1.13 μmol h^{-1}). By the way, the detector exhibits reproducible and flexible properties, as well as an enhanced photosensitive performance. The results will be helpful for the construction of hierarchical structures used in the PEC detectors.

Conflicts of interest

The authors declare no competing financial interest.

Acknowledgements

This work was supported by the National Key Research and Development Program of China (Grant No. 2017YFB0403101), the National Natural Science Foundation of China (Grant 61604127, 61474096).

References

1 W. A. Gil, A. M. Mahadeo, S. C. Weon, G. K. Hyun, C. Min and S. J. Jum, Enhanced solar photoelectrochemical conversion efficiency of the hydrothermally-deposited TiO_2 nanorod arrays: Effects of the light trapping and optimum charge transfer, *Appl. Surf. Sci.*, 2018, **440**, 688–699.
2 L. Bin and S. A. Eray, Growth of oriented single-crystalline rutile TiO_2 nanorods on transparent conducting substrates for dye-sensitized solar cells, *J. Am. Chem. Soc.*, 2009, **131**, 3985–3990.
3 W. X. Guo, C. Xu, X. Wang, S. H. Wang, C. F. Pan, C. J. Lin and Z. L. Wang, Rectangular bunched rutile TiO_2 nanorod arrays grown on carbon fiber for dye-sensitized solar cells, *J. Am. Chem. Soc.*, 2012, **134**, 4437–4441.
4 G. Q. Chang, Z. Cheng, R. Warren, G. X. Song, J. Y. Shen and L. W. Lin, Highly efficient photocatalysts for surface hybridization of TiO_2 nanofibers with carbon films, *ChemPlusChem*, 2015, **80**, 827–831.
5 X. Cai, H. W. Wu, H. C. Hou, M. Peng, X. Yu and D. C. Zou, Dye-sensitized solar cells with vertically aligned TiO_2 nanowire arrays grown on carbon fibers, *ChemSusChem*, 2014, **7**, 474–482.

6 P. K. Sharma, M. A. L. R. M. Cortes, J. W. J. Hamiltona, Y. S. Han, J. A. Byrne and M. Nolan, Surface modification of TiO_2 with copper clusters for band gap narrowing, *Catal. Today*, 2019, **321–322**, 9–17.

7 Z. M. Zhao, J. Sun, G. J. Zhang and L. J. Bai, The study of microstructure, optical and photocatalytic properties of nanoparticles (NPs)-Cu/TiO_2 films deposited by magnetron sputtering, *J. Alloys Compd.*, 2015, **652**, 307–312.

8 H. Masai, T. Miyazaki, K. Mibu, Y. Takahashi and T. Fujiwara, Phase separation and the effect of SnO addition in TiO_2-precipitated glass-ceramics, *J. Eur. Ceram. Soc*, 2015, **35**, 2139–2144.

9 L. X. Liu, G. C. Fan, J. R. Zhang and J. J. Zhu, Ultrasensitive cathode photoelectrochemical immunoassay based on TiO_2 photoanode-enhanced 3D Cu_2O nanowire array photocathode and signal amplification by biocatalytic precipitation, *Anal. Chim. Acta*, 2018, **1027**, 33–40.

10 G. D. Moon, J. B. Joo, I. Lee and Y. Yin, Decoration of size-tunable CuO nanodots on TiO_2 nanocrystals for noble metal-free photocatalytic H_2 production, *Nanoscale*, 2014, **6**, 12002–12008.

11 R. Naeem, M. A. Ehsan, A. Rehman, Z. H. Yamani, A. S. Hakeem and M. Mazhar, Single step aerosol assisted chemical vapor deposition of p–n Sn(II) oxide–Ti(IV) oxide nanocomposite thin film electrodes for investigation of photoelectrochemical properties, *New J. Chem.*, 2018, **42**, 5256–5266.

12 P. Pathak, S. Gupta, K. Grosulak, H. Imahori and V. Subramanian, Nature-inspired tree-like TiO_2 architecture: a 3D platform for the assembly of CdS and reduced graphene oxide for photoelectrochemical processes, *J. Phys. Chem. C*, 2015, **119**, 7543–7553.

13 O. M. Berengue, R. A. Simon, A. J. Chiquito, C. J. Dalmaschio, E. R. Leite, H. A. Guerreiro and F. E. G. Guimaraes, Semiconducting Sn_3O_4 nanobelts: growth and electronic structure, *J. Appl. Phys.*, 2010, **107**, 033717.

14 W. W. Xia, H. B. Wang, X. H. Zeng, J. Han, J. Zhu, M. Zhou and S. D. Wu, High-efficiency photocatalytic activity of type II SnO/Sn_3O_4 heterostructures *via* interfacial charge transfer, *CrystEngComm*, 2014, **16**, 6841–6847.

15 Y. H. He, D. Z. Li, J. Chen, Y. Shao, J. J. Xian, X. Z. Zheng and P. Wang, Sn_3O_4: a novel heterovalent-tin photocatalyst with hierarchical 3D nanostructures under visible light, *RSC Adv.*, 2014, **4**, 1266–1269.

16 H. Song, S. Y. Son, S. K. Kim and G. Y. Jung, A facile synthesis of hierarchical Sn_3O_4 nanostructures in an acidic aqueous solution and their strong visible light-driven photocatalytic activity, *Nano Res.*, 2015, **8**, 3553–3561.

17 X. Yu, Z. H. Zhao, N. Ren, J. Liu, D. H. Sun, L. H. Ding and H. Liu, Top or Bottom, Assembling modules determine the photocatalytic property of the sheet like nanostructured hybrid photocatalyst composed with Sn_3O_4 and rGO (GQD), *ACS Sustainable Chem. Eng.*, 2018, **6**, 11775–11782.

18 X. Yu, L. F. Wang, J. Zhang, W. B. Guo, Z. H. Zhao, Y. Qin, X. N. Mou, A. X. Li and H. Liu, Hierarchical hybrid nanostructures of Sn_3O_4 on N doped TiO_2 nanotubes with enhanced photocatalytic performance, *J. Mater. Chem. A*, 2015, **3**, 19129–19136.

19 L. P. Zhu, H. Lu, D. Hao, L. L. Wang, Z. H. Wu, L. J. Wang, P. Li and J. H. Ye, Three-dimensional lupinus-like TiO_2 nanorod@Sn_3O_4 nanosheet hierarchical heterostructured arrays as photoanode for enhanced photoelectrochemical performance, *ACS Appl. Mater. Interfaces*, 2017, **9**, 38537–38544.

20 G. H. Chen, S. Z. Ji, Y. H. Sang, S. J. Chang, Y. N. Wang, P. Hao, J. Claverie, H. Liu and G. W. Yu, Synthesis of scaly Sn_3O_4/TiO_2 nanobelt heterostructures for enhanced UV-visible light photocatalytic activity, *Nanoscale*, 2015, **7**, 3117.

21 W. J. Lee and M. H. Hon, An ultraviolet photo-detector based on TiO_2/water solid–liquid heterojunction, *Appl. Phys. Lett.*, 2011, **99**, 251102.

22 W. W. Xia, H. Y. Qian, X. H. Zeng, J. Dong, J. Wang and Q. Xu, Visible-light self-powered photodetector and recoverable photocatalyst fabricated from vertically aligned Sn_3O_4 nanoflakes on carbon paper, *J. Phys. Chem. C*, 2017, **121**, 19036–19043.

23 X. D. Li, C. T. Gao, H. G. Duan, B. G. Lu, X. J. Pan and E. Q. Xie, Nanocrystalline TiO_2 film based photoelectrochemical cell as selfpowered UV-photodetector, *Nano Energy*, 2012, **1**, 640–645.

24 Z. R. Wang, S. H. Ran, B. Liu, D. Chen and G. Z. Shen, Multilayer TiO_2 nanorod cloth/nanorod array electrode for dye-sensitized solar cells and self-powered UV detectors, *Nanoscale*, 2012, **4**, 3350–3358.

25 C. T. Gao, X. D. Li, X. P. Zhu, L. L. Chen, Y. Q. Wang, F. Teng, Z. X. Zhang, H. G. Duan and E. Q. Xie, High performance, self-powered UV-photodetector based on ultrathin, transparent, SnO_2–TiO_2 core–shell electrodes, *J. Alloys Compd.*, 2014, **616**, 510–515.

26 W. W. Xia, H. Y. Qian, X. H. Zeng, J. Dong, J. Wang and Q. Xu, Visible-light self-powered photodetector and recoverable photocatalyst fabricated from vertically aligned Sn_3O_4 nanoflakes on carbon paper, *J. Phys. Chem. C*, 2017, **121**, 19036–19043.

27 R. Kodiyath, J. J. Wang, T. Hara, A. Dakshanamoorthy, S. Ishihara, K. Ariga, J. H. Ye, N. Umezawa, H. Abe, *et al.*, Photocatalytic water splitting under visible light by mixed-valence Sn_3O_4, *ACS Appl. Mater. Interfaces*, 2014, **6**, 3790–3793.

28 P. A. DeSario, J. J. Pietron, D. H. Taffa, R. Compton, S. Schünemann, R. Marschall, T. H. Brintlinger, R. M. Stroud, M. Wark, J. C. Owrutsky and D. R. Rolison, Correlating changes in electron lifetime and mobility on photocatalytic activity at network-modified TiO_2 aerogels, *J. Phys. Chem. C*, 2015, **119**, 17529–17538.

29 L. M. Peter and K. G. U. Wijayantha, Intensity dependence of the electron diffusion length in dye-sensitised nanocrystalline TiO_2 photovoltaic cells, *Electrochem. Commun.*, 1999, **1**, 576–580.